

See discussions, stats, and author profiles for this publication at: <https://www.researchgate.net/publication/51689360>

Structure of the Molten Salt Methyl Ammonium Nitrate Explored by Experiments and Theory

ARTICLE in THE JOURNAL OF PHYSICAL CHEMISTRY B · OCTOBER 2011

Impact Factor: 3.3 · DOI: 10.1021/jp2070002 · Source: PubMed

CITATIONS

21

READS

58

8 AUTHORS, INCLUDING:



Enrico Bodo

Sapienza University of Rome

111 PUBLICATIONS 1,536 CITATIONS

SEE PROFILE



Paolo Postorino

Sapienza University of Rome

158 PUBLICATIONS 2,061 CITATIONS

SEE PROFILE



Giovanni Piacente

Università degli Studi dell'Aquila

4 PUBLICATIONS 35 CITATIONS

SEE PROFILE



Paolo Ballirano

Sapienza University of Rome

145 PUBLICATIONS 1,157 CITATIONS

SEE PROFILE

Structure of the Molten Salt Methyl Ammonium Nitrate Explored by Experiments and Theory

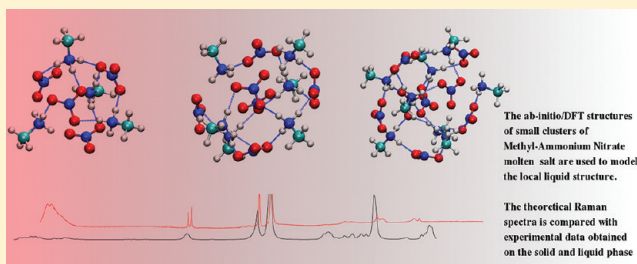
E. Bodo,^{*,†} P. Postorino,^{‡,||} S. Mangialardo,[‡] G. Piacente,[‡] F. Ramondo,[‡] F. Bosi,[§] P. Ballirano,[§] and R. Caminiti[†]

[†]Department of Chemistry and CNISM, [‡]Department of Physics, and [§]Department of Earth Sciences, University of Rome "La Sapienza", P. A. Moro 5, 00185, Rome, Italy

^{||}National Institute of Nuclear Physics (INFN), Via Enrico Fermi, 40-00044 Frascati, Rome, Italy

[‡]Department of Chemistry, Chemical Engineering and Materials, University of L'Aquila, via Vetoio, Coppito, I 67100 L'Aquila, Italy

ABSTRACT: We present an analysis of the structure of the monomethylammonium nitrate (MMAN) compound. Vibrational Raman spectroscopy and X-ray powder diffraction have been used to characterize the bulk phases of MMAN, and assignment of the resonant frequencies has been performed by ab initio (DFT) computations on small clusters of the compound. The theoretical spectra are in excellent agreement with the experimental ones and provide a means by which an interpretation of the hydrogen-bonding network that exists in such compound can be analyzed. In particular, we found that the spectrum of one of the solid phases is structurally very similar to that of the liquid. We present experimental evidence for the existence of such phase both from X-ray data and Raman spectra which, in turn, is easily interpreted with a one-to-one correspondence with the ab initio simulation of the small clusters. A geometric structure of the short-range local arrangement in these two bulk phases is therefore proposed.



INTRODUCTION

Among the most exciting and successful materials developed and studied in the last 20 years, ionic liquids^{1,2} are part of those that can certainly claim one of the most rich fields of applications in industry and in applied technological research. Their long story lays its roots in the molten salts research field and can be traced back to 1914 with the synthesis of ethylammonium nitrate by Paul Walden. Looking at the evolution of this research field, one can see a remarkably parallel development between academic research and industrial applications.³ In addition to their appeal for technology, ionic liquids remain a crucial subject of academic and nonapplied research because they represent unconventional fluids that defy a simple description under many points of view.^{1,2,4} These substances contain both an organic cation (which can, for example, be an asymmetric derivative of the 1-alkylpyridinium, tetraalkylphosphonium, or 1,3-dialkylimidazolium) and an inorganic anion. Their versatility depends on the fact that their properties can be tuned by varying the cation and the anion⁵ and their molecular structure. Despite the possibility of tuning some of the physical and chemical properties by ion substitution, a few common features are shared by almost all the members of this very large family of compounds: electrical conductivity, chemical and thermal stability, large liquidus range, and negligible vapor pressure.

Thanks to these properties, ionic liquids have soon been recognized⁶ as ideal candidates for many and diverse applications. The large variety of applications includes their use as a "green"

replacement of organic solvents,^{4,7} lubricants,⁸ ingredients for pharmaceuticals,^{9–11} reaction media,^{12–15} extraction media in analytical chemistry^{16–18} and solvents for electrochemistry.^{19–22}

Recently, development of suitably tailored atomistic simulation techniques and parallel growth of computational power have reached the point in which it is possible to reliably provide by simulations a nanoscopic interpretation of the bulk properties of these materials.²³ Theoretical modeling plays a crucial role in ionic liquid research as a mean for rationalization of the experimental observations and as a valuable tool in designing new ionic liquid systems with properties optimized for specific technological applications.

An appealing subset of ionic liquids are protic ionic liquids (PILs) that can be prepared by combination of Brønsted acids and bases.^{24–27} A key feature in PILs is possible proton transfer from acid to base (proton transfer rarely takes place in the bulk, liquid, or solid phase but is thought to be the main evaporation mechanism whereby an ionic couple reacts and gives rise to a couple of volatile neutral molecules), leading to formation of proton acceptor and donor sites that eventually will lead to a hydrogen-bonded network. These features make PILs appealing candidates for new generation fuel cells electrolytes.²⁸ To date, the understanding of PILs performances is very limited. It is well

Received: July 22, 2011

Revised: September 21, 2011

Published: October 03, 2011

known that their properties strongly depend on the acid–base equilibrium and, consequently, temperature. It is remarkable however that major issues such as ion–ion interactions, ionic transport, and structural correlations are still far from having been elucidated.

Alkylammonium nitrates are among the most studied PILS,^{29–31} and monomethylammonium nitrate (MMAN), in particular, is one of the first ionic liquids ever synthesized.³² It was recently observed that such PILS (with chain larger than methyl) present some kind of long-range ordering over the nanometer spatial scale:²⁹ this structural organization is thought to stem from self-assembly of the apolar alkyl chains into a charged (as well as hydrogen-bonded) network.

MMAN represents the ultimate prototype of protic ionic liquids for its simplicity and has been studied extensively in the past from both experimental and theoretical points of view. In particular, it exists in three phases: solid II below 352 K, solid I between 352 and 391 K, and liquid above 391 K. It is also known from NMR measurements³³ that the solid I and liquid phases are equally disordered and that in these phases the nitrate anions and methylammonium cations are undergoing rapid end-over-end rotations (the solid of this kind, where the ions are often termed “ionic plastic”). More recently, there has been an *ab initio* molecular dynamics analysis of MMAN^{34,35} which led to the following conclusions

- proton transfer is inhibited on a picosecond time scale,
- there is no nanoscale segregation due to the alkyl “chain” being too small,
- the hydrogen bonds between cation and anion are directional and use 1.8 contacts over the possible 3,
- the orientation network is different from water because of the 3-fold symmetries of the donor and acceptor sites,
- the relatively tight bound ionic couples have a lifetime that spans the simulation time (tens of picoseconds).

In the present work, we present an experimental analysis of the three bulk phases by means of Raman spectroscopy, X-ray powder diffraction data, and an interpretation of the spectra obtained by *ab initio* analysis of few small clusters of the ionic liquid.

EXPERIMENTAL AND COMPUTATIONAL METHODS

X-ray Single-Crystal Structural Refinement (SREF). MMAN purchased from Iolitech (product IL-01245-SG) was used as a starting material. A few crystals of MMAN were selected for X-ray single-crystal structure analysis. Complete intensity data were collected, under room conditions, at the X-ray Diffraction Laboratory of the University of Rome “La Sapienza” using a Bruker AXS KAPPA APEX-II diffractometer equipped with a CCD area detector ($6.2 \times 6.2 \text{ cm}^2$ active detection area, 512×512 pixels) and a graphite crystal monochromator using Mo $K\alpha$ radiation from a fine-focus sealed X-ray tube. The sample to detector distance was 4 cm. A total of 2028 exposures (step = 0.25° , time/step = 25 s) covering a full reciprocal sphere with a high redundancy of about 18 were collected, and a completeness of 99.7% was achieved. The orientation of the crystal lattice was determined using more than 800 strong reflections ($I > 100\sigma_I$) evenly distributed in reciprocal space and used for subsequent integration of all recorded intensities. Final unit-cell parameters, $a = 10.4079(14) \text{ \AA}$, $b = 6.5701(8) \text{ \AA}$, and $c = 6.4038(9) \text{ \AA}$, were refined using the Bruker AXS SAINT program on reflections with $I > 10\sigma_I$ in the range $5^\circ < 2\theta < 55.03^\circ$. The intensity data were processed and corrected for Lorentz, polarization, and

Table 1. Crystal Data for MMAN

chemical formula	CH ₃ NH ₃ NO ₃
wavelength (Å)	0.71073
space group	<i>Pnma</i>
<i>Z</i>	4
cell parameters (Å)	$a = 10.4079(14)$, $b = 6.5701(8)$, $c = 6.4038(9)$
volume (Å ³)	437.90(1)
crystal sizes (mm)	$0.12 \times 0.30 \times 0.35$
2θ max (deg)	55.03
index ranges	$-11 \leq h \leq 13$, $8 \leq k \leq 7$, $8 \leq l \leq 8$
reflins collected	4189
independent reflns	546 [$R_{\text{int}} = 0.0370$]
completeness (%)	99.7

Table 2. Miscellaneous Data of the Refinements

	harmonic	anharmonic
R_{obs}	4.18	2.92
$R_{\text{w,obs}}$	8.87	5.76
R_{all}	7.69	6.44
$R_{\text{w,all}}$	9.35	6.45
N_{obs}	322	
N_{all}	546	
ref params	49	71
GOF(obs)	2.42	1.64
GOF(all)	1.89	1.34

background effects with the APEX2 software program of Bruker AXS. Data were corrected for absorption using the multiscan method (SADABS). Absorption correction led to a significant improvement in R_{int} . Details on data collection are reported in Table 1. Structure refinements were carried out with Jana2006.³⁶ Refinements was performed on *Pnma* using as starting parameters those of Mylrajan et al.³⁷ after matrix transformation (001, 010, 100) from *Pcmn* to *Pnma*. A first refinement carried out with anisotropic displacement parameters for all non-hydrogen atoms converged to fairly good agreement indices. A second refinement performed allowing anharmonic motion for the NO₃[−] group provided a significant reduction of the agreement indices (Table 2). The importance of the anharmonic motion for NO₃[−] has been already reported by Gonschorek et al.³⁸ in NaNO₃ nitratine structural determination

Nonambient X-ray Powder Diffraction (XRPD). A preliminary powder diffraction pattern on a conventional Bragg–Brentano instrument confirmed the absence of detectable impurities. The material was gently ground in a mortar. The powder was loaded in a 0.7 mm diameter borosilicate-glass capillary that was closed and glued to a 1.2 mm outer (1.0 mm inner) diameter Al₂O₃ tube by means of an high-purity alumina ceramic (Resbond 989). The capillary/tube assembly was subsequently aligned onto a standard goniometer head.

Nonambient data were collected on a parallel-beam Bruker AXS D8 Advance diffractometer operating in θ – θ geometry, fitted with two Soller slits (4° opening angle on the incident and radial on the diffracted beam) and a PSD VÅNTEC-1 detector set to a 6° 2θ aperture. The capillary heating chamber is a prototype developed with MRI and AXS Bruker.³⁹ The sample was heated from 303 to 385 K with a T step of 4 K in the 303–351 K range

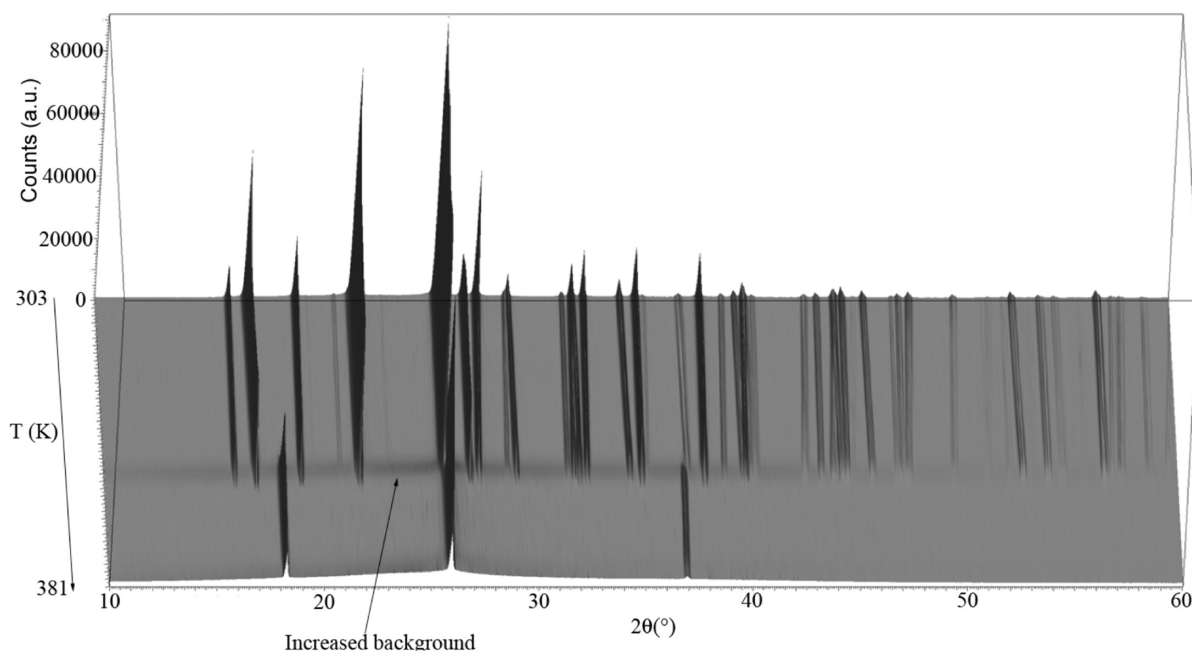


Figure 1. Magnified view of the complete data set shown as a 3D plot. Arrow indicates the increase of the background.

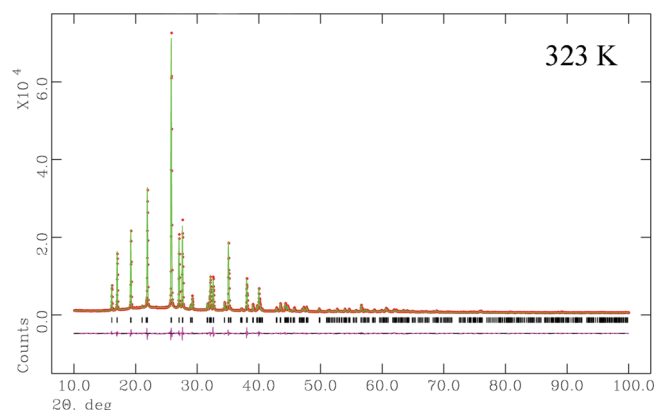


Figure 2. Fitted X-ray diffraction patterns obtained at 323 K. The lower curve represents the difference between observed and calculated profiles. Vertical marks refer to the position of calculated Bragg reflections.

and of 2 K in the 351–385 K thermal range. The investigated angular range was 3–100° 2θ , step size 0.022° 2θ , 2 s counting time, using Cu $K\alpha$ radiation. A magnified view of the full data set is reported in Figure 1 as a 3D plot. Scrutiny of the data set indicates that a phase transition occurs at 351 K coupled with a significant increase of the background. Data were evaluated with the GSAS suite of programs⁴⁰ coupled with the EXPGUI graphical user interface.⁴¹ Peak shape was modeled by a pseudo-Voigt function⁴² modified to incorporate asymmetry.⁴³ The peak cutoff was set to 0.2% of the peak maximum, and background was fit with a 36-term Chebyshev polynomial of the first kind. An absorption parameter, including the contribution from the aluminum heating chamber windows, was determined at 303 K and kept fixed at that value for nonambient data. Starting structural data were taken from the RT single-crystal work. However, structure refinement of the data at 303 K indicated the necessity to refine anisotropically the non-hydrogen atoms in order to achieve good statistical indicators. Therefore, due to the inability to perform stable anisotropic

refinements throughout the analyzed thermal range we decided to keep fixed the structure and refine cell parameters only. It should be reminded that despite this limitation very good fitting was obtained at each investigated temperature, indicating that only marginal structural arrangements occurred until the phase transition. An example of the Rietveld plots obtained for the diffraction pattern collected at 323 K is reported in Figure 2. For the solid I polymorph, three peaks were located by a profile-fitting technique using the Topas 4.2 software.⁴⁴ A solution was easily obtained in the cubic system for $a = 4.872(1)$ Å, volume = 115.64(1) Å³. The volume, which is approximately 1/4 of that of the solid II phase, is consistent with $Z = 1$. The three 001, 111, 002 reflections indicate the lack of reflection conditions consistent with the extinction symbol P ——. Therefore, candidate space groups were $P23$, $Pm\bar{3}$, $P432$, $P\bar{4}3m$, and $Pm\bar{3}m$. The dependence of the cubic a -cell parameter from temperature was investigated by Le Bail fitting of the data.

■ RAMAN MEASUREMENTS

Raman measurements were carried out using a confocal-microscope Raman spectrometer, equipped with a set of interchangeable objectives with long working distances and different magnifications from 4× to 100×. Samples were excited by the 632.8 nm line of a 20 mW HeNe laser. The 1800 lines/mm grating monochromator and a charge-coupled-device (CCD) detector allowed for a spectral resolution better than 3 cm^{−1}. Elastically scattered light was removed by a holographic notch filter which avoided collecting spectra within the low-frequency spectral region. Raman spectra were indeed collected in backscattering geometry over different spectral ranges spanning from 300 to 3800 cm^{−1}. Using thin-walled quartz cuvettes and a sample heater temperature-dependent measurements were collected over the temperature range of about 300–400 K. Use of a rather small confocal diaphragm (<100 μm) allowed us to minimize the contribution arising from the quartz windows. Polarization-dependent measurements were also carried out (not shown here) to distinguish

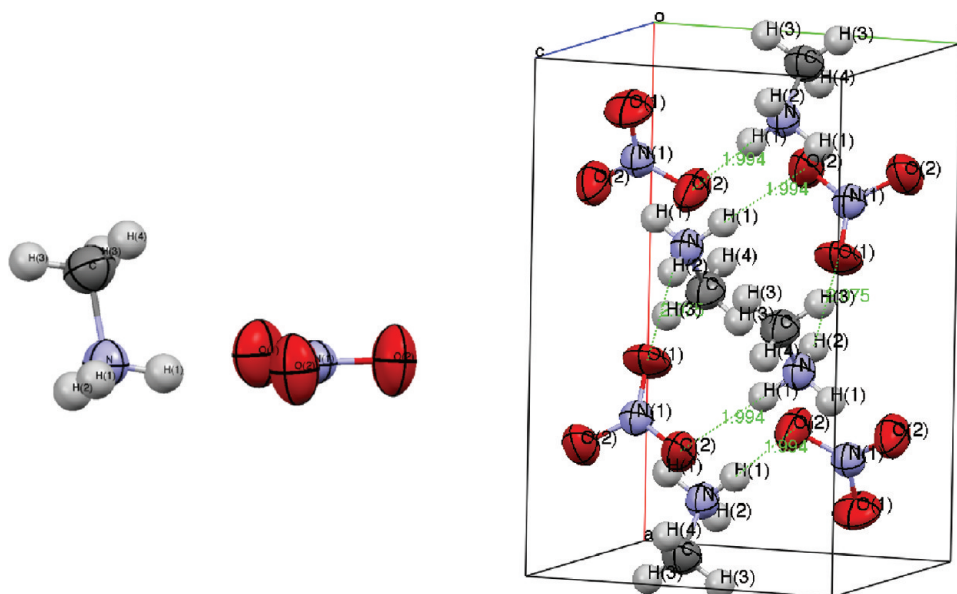


Figure 3. (Left) Asymmetric unit content. (Right) Molecular packing. Hydrogen bonds are sketched.

among peaks of different symmetries but with central frequencies too close to be clearly resolved.

MD Annealing and Quantum Calculations. When the number of atoms in a molecular system increases, the number of local minima of the potential energy surface (PES) becomes quickly so large that a systematic search is impossible. In other words, the large number of internal degrees of freedom prevents exploration of the PES in all possible geometries of the system. Therefore, one of the main computational problems in the study of the stable geometries of complex molecular systems, especially those characterized by a high conformational mobility, is that of locating possible good candidates for the time-consuming, *ab initio* optimizations. One possible approach, in relatively small systems, is that of generating randomly (or by chemical intuition) many different starting structures (see ref 18 for an example of such procedure) and optimize them separately. However, this route is impracticable in the compounds that are the target of this work because of the large number of initial, realistic geometric guesses which exist. There are many theoretical methodologies that, in an initial stage, bypass the quantum problem and can help in discovering the lower lying minima over a complex PES for system composed by many atoms: these methods are based on Monte Carlo (MC) sampling,⁴⁵ molecular dynamics (MD), or genetic algorithm searches.⁴⁶ Here, we adopted the MD method to provide a reasonable starting structure for subsequent *ab initio* optimizations. We employed the OPLS force field⁴⁷ with nitrate parameters obtained by ref 48 and used the tinker⁴⁹ package in order to locate various “classical” minima on the PES. Our recipe is the following: we start with a small cluster of ionic couples. We run a 100 ns molecular dynamics trajectory at 150–200 K with a 1 fs time step saving a snapshot of the system each 1000 steps. We then minimize each snapshot and locate a few minimum energy structures for which we repeat the dynamics but with a lower temperature. At this point, we are generally able to locate a recurring structure that, very likely, is the global minima for the adopted force field. In order to further test the lowest energy structures, we have run, for some of the absolute minima, a Monte Carlo minimum search as implemented in the tinker

Table 3. Fractional Coordinates and Equivalent/Isotropic Displacement Parameters of MMAN^a

atom	<i>x</i>	<i>y</i>	<i>z</i>	<i>U</i> _{eq} (Å ²)
N(1)	0.2055(2)	1/4	0.7624(3)	0.0499(7)
	0.2027(5)	1/4	0.7654(6)	0.0498(7)
O(1)	0.09985(17)	1/4	0.8449(3)	0.0816(8)
	0.0991(3)	1/4	0.8475(5)	0.0828(7)
O(2)	0.25856(11)	0.41161(19)	0.7159(2)	0.0796(6)
	0.25789(18)	0.4109(4)	0.7165(3)	0.0787(5)
C	0.4964(3)	1/4	0.1694(5)	0.0650(12)
	0.4964(2)	1/4	0.1693(4)	0.0648(8)
N	0.4017(2)	1/4	0.3366(4)	0.0530(8)
	0.40170(17)	1/4	0.3363(3)	0.0530(6)
H(1)	0.3504(18)	0.364(3)	0.318(3)	0.086(6)
	0.3502(13)	0.360(2)	0.3202(19)	0.086(5)
H(2)	0.450(3)	1/4	0.456(6)	0.109(12)
	0.441(2)	1/4	0.456(4)	0.092(8)
H(3)	0.5485(19)	0.130(3)	0.192(3)	0.083(6)
	0.5475(14)	0.132(2)	0.189(2)	0.084(4)
H(4)	0.449(3)	1/4	0.044(6)	0.112(12)
	0.450(2)	1/4	0.039(4)	0.113(9)

^a *U*_{eq} defined as one-third of the trace of the orthogonalized *U*_{*ij*} tensor. First raw harmonic, second raw anharmonic refinement.

package, and it was impossible to achieve a lower energy. The global minima has then been optimized by means of the *ab initio* DFT method, and its IR and Raman absorption spectra (in the harmonic approximation) have then been calculated at the B3LYP/6-311G(d) and B3LYP/6311+G(d) levels using the Gaussian program.⁵⁰

Obviously, given the high number of local minima, we cannot be sure whether we are describing the global minima over the potential energy surface of these complexes or a local one. However, the MD-based annealing procedure described above should be certainly able to produce reasonable structures, so that

Table 4. Relevant Bond Distances (Å) and Angles (deg)

	harmonic	anharmonic
N(1)–O(1)	1.220(3)	1.200(6)
N(1)–O(2) × 2	1.2333(17)	1.243(4)
C–N	1.456(4)	1.454(3)
C–H(3)	0.97(2)	0.948(15)
C–H(4)	0.94(4)	0.97(3)
hydrogen bond		
N–H(1)	0.93(2)	0.906(15)
N...O(2)	2.885(2)	2.883(3)
H(1)...O(2)	1.97(2)	1.992(15)
N–H(1)...O(2)	168.0(16)	167.1(12)
N–H(2)	0.91(4)	0.87(2)
N...O(1)	2.901(3)	2.884(4)
H(2)...O(1)	2.02(4)	2.07(2)
N–H(2)...O(1)	162(3)	156(2)

we deem the following *ab initio* analysis to describe realistically all of the key structural features of the complexes.

■ RESULT AND DISCUSSION

RT X-ray Single-Crystal Refinement (SREF). The asymmetric unit content with atomic labeling is reported in Figure 3 along with the molecular packing. Fractional coordinates and equivalent/isotropic displacement parameters are listed in Table 3; anisotropic displacement parameters and those of the Gram–Charlier expansion for anharmonic motion are available upon request to P.B. The relevant bond distances and H-bonding features are reported in Table 4. The refinement confirms the findings of ref 37. It should be reminded that aspherical densities of atomic charges may, in some cases, be represented by anharmonic motion parameters.⁵¹ However, anharmonic motion for the NO₃[−] group has been refined and found to significantly increase as a function of *T* in nitratine NaNO₃.^{38,52} A few subtle differences were observed in the geometry of the nitrate group arising from anharmonic treatment. The effect of the relevant anharmonicity is to increase the difference between the N(1)–O(1) and the N(1)–O(2) bond distances to 1.200(6) and 1.243(4) Å, respectively. O(2) makes a contact of 3.047 Å with N that could be the reason for the elongation of the N(1)–O(2) bond as compared to the N(1)–O(1) one. The nitrate group is almost perfectly planar as the distance of the nitrogen atom from the O(1)–O(2)–O(2) mean plane is 0.013 Å. Moreover, it is worth noting that the thermal motion is almost perfectly normal to such plane (Figure 3). On the contrary, the H(1)···O(2) and H(2)···O(1) vectors are almost perfectly parallel to the O(1)–O(2)–O(2) mean plane (Figure 3). As a further result of the anharmonic approximation, the N–O(1) and N–O(2) distances become nearly identical. No differences at the 1σ level were observed for the fractional coordinates of the NH₃CH₃⁺ cation.

Thermal Expansion and Phase Transition. Thermal expansion of solid II MMAN has been investigated up to 351 K. In fact, at that temperature the structure converts to solid I MMAN characterized by a cubic symmetry (see Figure 4a). Conversion is coupled with a significant increase of the background, arising from diffuse scattering, suggesting the onset of a structural phase

with an intrinsic configurational disorder. Cell parameters and volume dependence from temperature closely follow a linear behavior as shown in Figure 4b. However, thermal expansion is significantly anisotropic and in the case of the *a*-cell parameters is negative, i.e., it contracts on heating. The unit cell parameters and volume dependence from *T* were fitted with a first-order polynomial $y = q + mT$, where *q* is the value of the corresponding parameter at 0 K and *m* is the first-order coefficient of expansion and *T* the temperature in Kelvin. The calculated parameters in the 303 K < *T* < 347 K range are shown in Table 5. The relative expansion of the cell parameters and volume are reported in Figure 4c. It is interesting to note that the *a*-axis contraction is almost perfectly counterbalanced by the *b*-axis expansion, so that the volume relative expansion is approximately of the same magnitude of that of the *c* axis. In an attempt to justify the contraction of the *a* cell parameter, it is worth noting that the hydrogen bonds have a significant component along the *a* axis.

At 351 K MMAN undergoes a solid II → solid I phase transition that is coupled with a significant increase of structural disorder. The new structure is cubic, candidate space groups *P23*, *Pm3*, *P432*, *P43m*, and *Pm3m*. It is worth noting that above RT ammonium nitrate shows a similar sequence of phase transition (III)_{305K}s.g.*Pnma* → (II)_{357K}s.g.*Pmbn* → (I)_{398K}s.g.*Pm3m*.⁵³ An attempt to define the structure of the solid I modification of MMAN failed because of the occurrence of three reflections only and possibly because of the expected large rotational disorder of both the anion and the cation, which is in agreement with previous findings from NMR measurements³³ and with the increase of the background signal in the present X-ray determination. A tentative model built in s.g. *Pm3m*, consisting of N at (a) and (b) Wyckoff sites and O and C disordered at (g), produced fairly good agreement indices. The dependence of the cubic *a* cell parameter from temperature, investigated by Le Bail fitting of the data, indicates a regular linear expansion Figure 4d. Similar to solid II MMAN, the *a* unit cell parameter and volume dependence from *T* of the solid I modification were fitted with the same first-order polynomial $y = q + mT$. The calculated parameters are shown in Table 5. The volumetric expansion is approximately of the same magnitude of solid II MMAN. However, it is important to realize that the volume of the solid I modification (multiplied by four to be rescaled to the same *Z* of solid II MMAN) undergoes a significant expansion (3.5%) at the transition temperature. Reference data³⁷ indicate the occurrence of a significant thermal hysteresis for the transition. In fact, during the heating process the transition has been reported to occur at 355 K, whereas on cooling the temperature is significantly lower, being of 330 K. Under the present experimental conditions, no such hysteresis has been observed as can be seen from Figure 5 on a further data set measured on a new capillary in the 343–353 and 351–343 K thermal ranges. The intensity differences observed for the solid II polymorph before and after the heating/cooling cycle are due to preferred orientation effects possibly arising from the “plastic” behavior of the solid I polymorph. Melting started at 381 K and was completed at 385 K.

Theory: “Classical” Structures. In order to check the reliability of the chosen force fields we have run a short molecular dynamics for the solid phase solid II MMAN starting from the structure determined by X-ray and reported above. We expanded the unit cell by 3,3,3 multiplication in the real space and performed an NPT 0.5 ns dynamic at ambient conditions. The

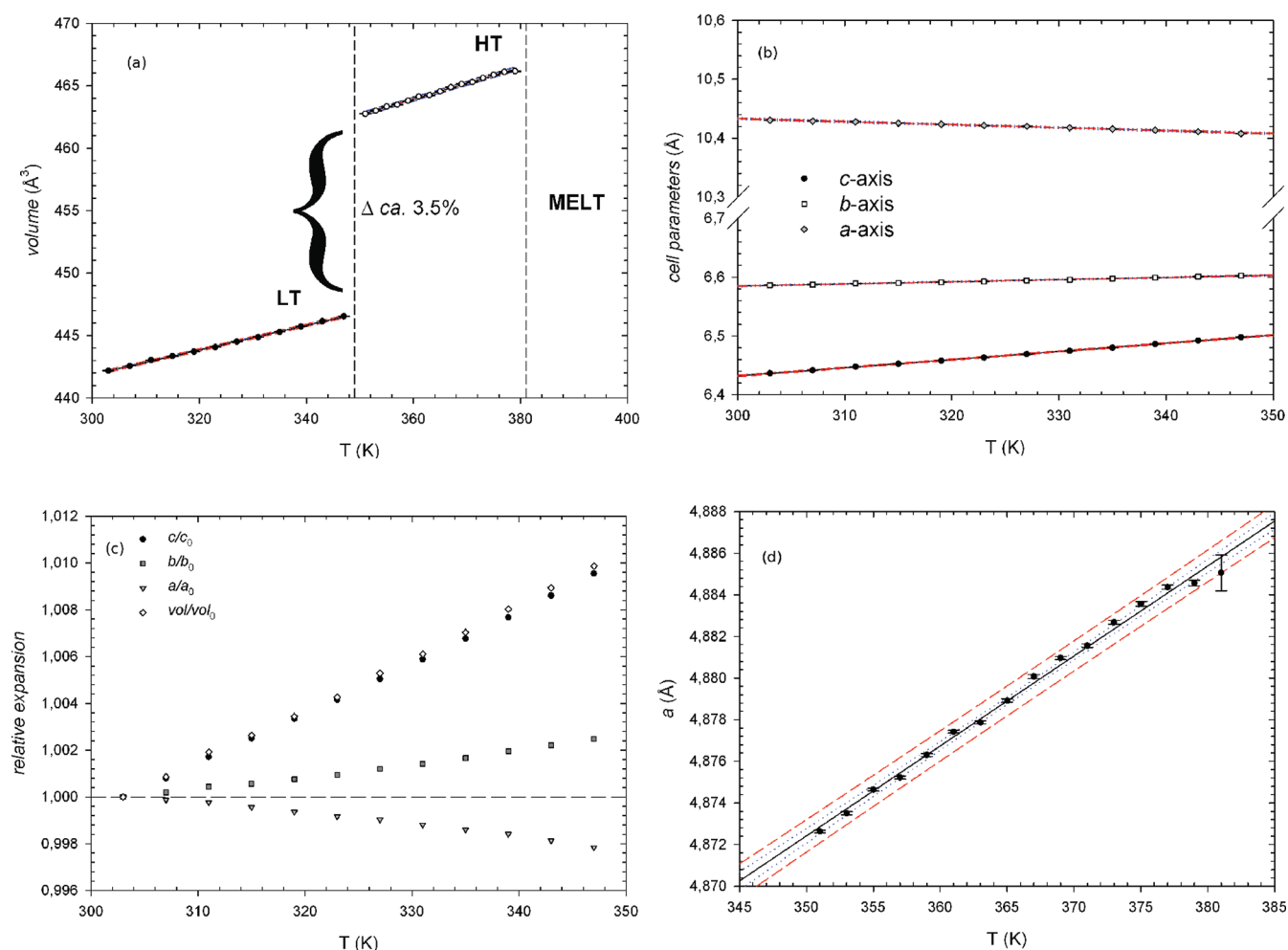


Figure 4. (a) Volume dependence of MMAN on temperature. (b) Cell parameters dependence on temperature for solid II MMAN. (c) Relative expansion of cell parameter and volume of solid I MMAN. (d) *a*-cell parameters temperature dependence of solid I MMAN.

equilibrated resulting structure had cell parameters of $a = 10.61$ Å, $b = 6.70$ Å, and $c = 6.53$ Å that are within 2% with the experimental cell parameters reported in Table 1 (OPLS default parameters gave slightly shorter values $a = 10.17$ Å, $b = 6.42$ Å, and $c = 6.26$ Å). Note however that upon heating our simulations were unable to reproduce the thermal expansion as determined experimentally; in particular, contraction of the *a*-cell parameter was not observed. The cluster structures resulting from our molecular dynamics approach are reported in Figure 6 for various numbers of ionic couples. In the structure with 4 ionic couples the hydrogen-bond network is clearly forming a sort of cubic “cage”. The resulting cluster has a highly symmetric structure, although we did not impose any restriction in the optimization process. The symmetry is lost in the $n = 5$ cluster and is partially recovered in the $n = 6$ one, although for the adopted force field one of the nitrate anions prefer to locate itself in the middle of the cluster, thereby preventing formation of a double cubic structure reminiscent of the $n = 4$ one. The $n = 8$ cluster shows again a very compact structure where the H bonds create a closed structure. As it is evident in the reported geometries, the methyl groups are pointing out with respect to the H-bond cage.

Contrary to what one may think, these structures are fairly rigid owing to the strong electrostatic interactions and the resulting

Table 5. Results from Linear Data-Fitting Procedures for the Thermal Expansion Data of MMAN Using the Polynomial $y = q + mT$

	<i>a</i>	<i>b</i>	<i>c</i>	volume
solid II MMAN				
R^2	0.9904	0.9933	0.9995	0.9992
<i>q</i>	10.555(5)	6.475(3)	6.016(3)	412.3(3)
<i>m</i>	$-5.06(16) \times 10^{-4}$	$3.67(9) \times 10^{-4}$	$1.39(1) \times 10^{-3}$	$9.86(9) \times 10^{-2}$
solid I MMAN				
R^2	0.9942			0.9967
<i>q</i>	4.721(3)			418.3(7)
<i>m</i>	$4.32(9) \times 10^{-4}$			$1.27(2) \times 10^{-1}$

H-bonding features. An idea of the “rigidity” of such clusters can be had by looking at the picture reported in Figure 7, where we reported a volumetric map of the nitrate ion averaged over all minima structures obtained from each MD snapshot superimposed on the absolute minimum energy ones. As can be seen, only the structure with $n = 8$ ionic pairs shows the presence of multiple minima which recur with sufficient frequency to provide a broad distribution of nitrate geometries. The nitrate distribution on the

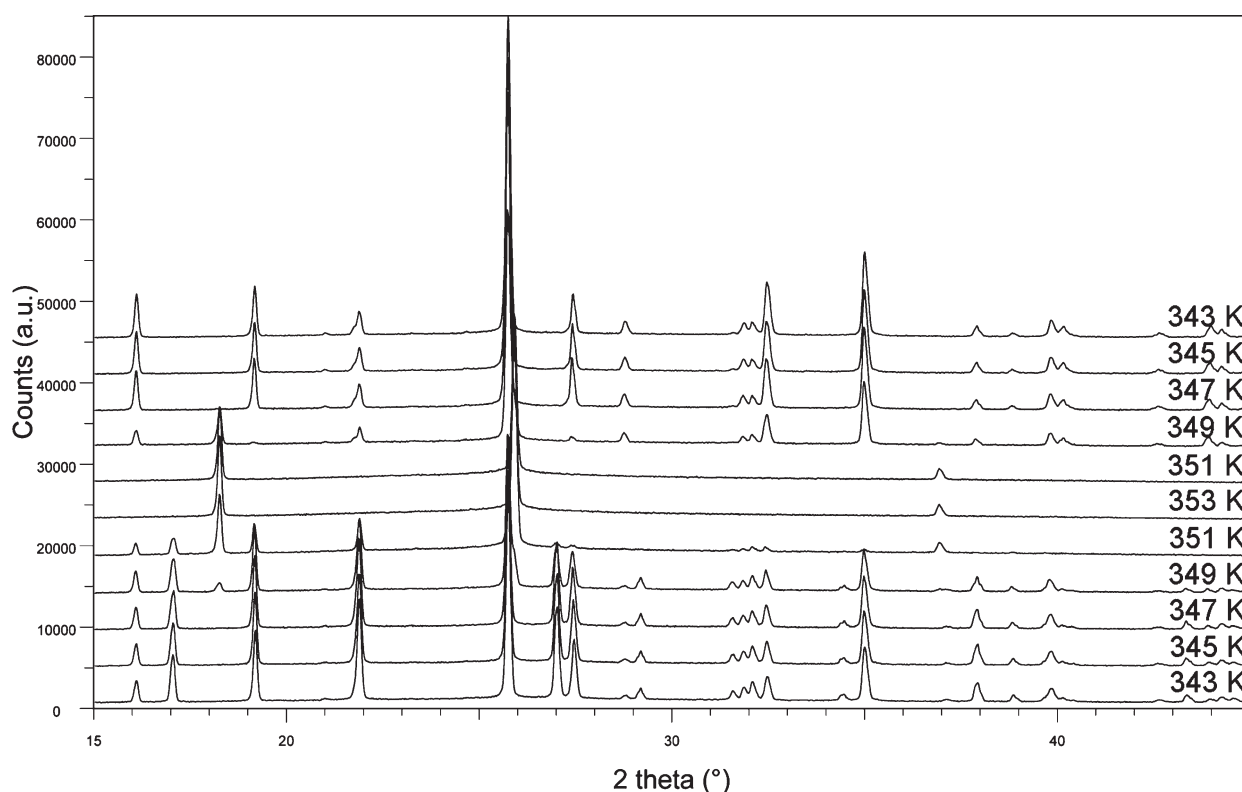


Figure 5. Diffraction patterns collected, from below to above, during a heating/cooling cycle from 343 to 353 K and from 353 to 343 K.

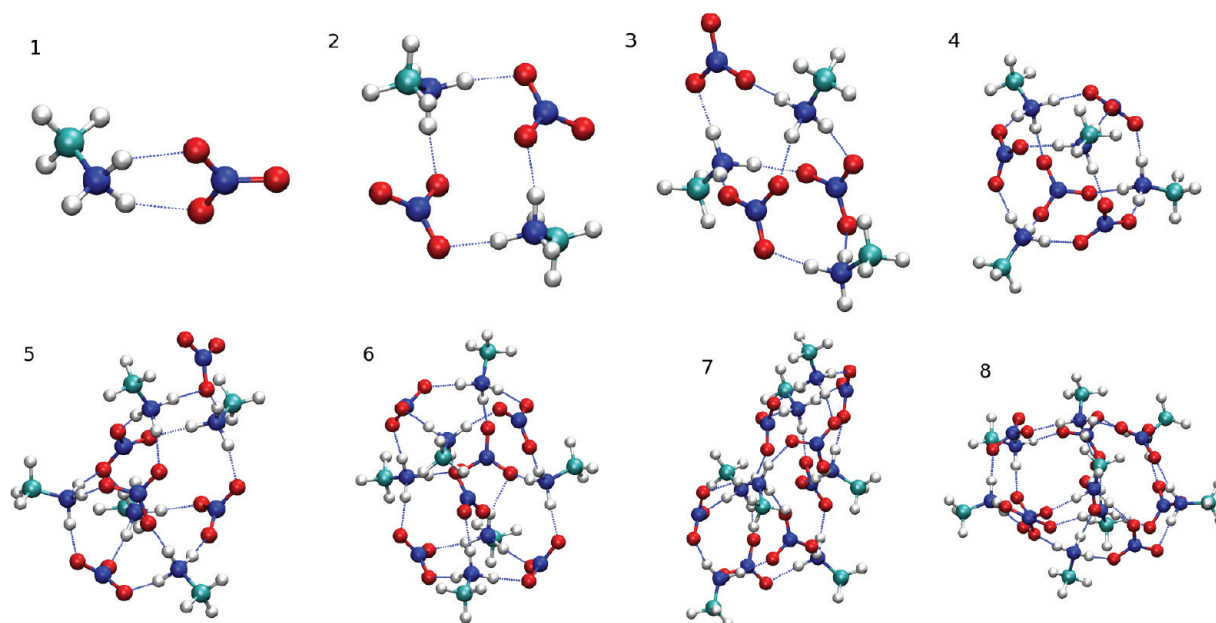


Figure 6. Minimum energy structure as resulting from MD minimization cycles. H bonds are represented by blue dotted lines and have been drawn for a radial cutoff of 3 Å and an angular cutoff of 40°.

$n = 4$ and 6 clusters is almost exclusively tetrahedral and pyramidal, respectively.

The average $\text{O}(\text{nitrate}) \cdots \text{N}(\text{ammonium})$ distances in all these clusters are between 2.67 and 2.72 Å (only larger clusters), and the $\text{O} \cdots \text{H}-\text{N}$ angle is between 167° and 173°, which is consistent with the standard definition of the H bond. As we shall

see below, while the angle is compatible with QM calculations and experiments described above (see Table 4), the $\text{O} \cdots \text{H}$ distance is slightly underestimated.

By taking the total potential energy differences between the structure along the growth pattern we can establish that at the OPLS level each new ionic couple brings an average of ~ 141 kcal

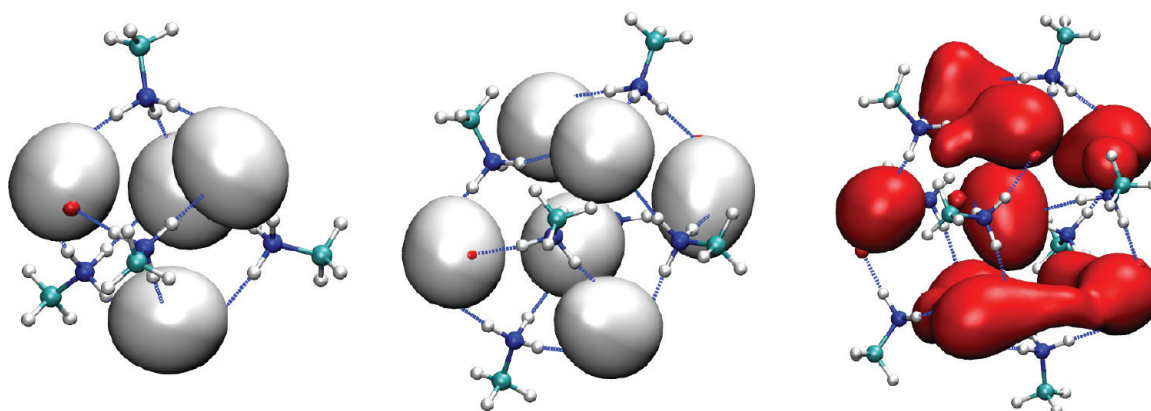


Figure 7. Minimum energy structure as resulting from MD minimization cycles superimposed to a volumetric map of the nitrate ions (bin size box 0.3 \AA^3 and cutoff density 0.2) obtained from all other minima that we found.

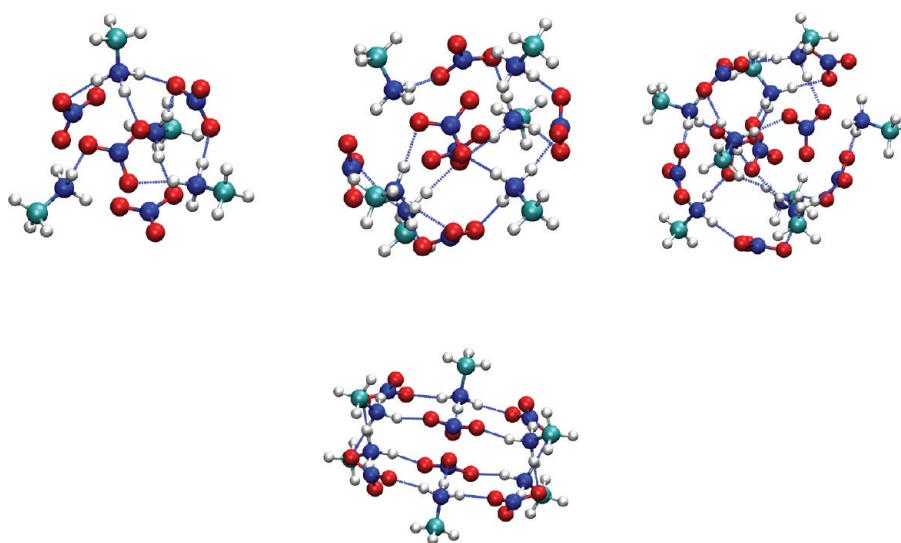


Figure 8. (Top) Minimum energy structure resulting from QM B3LYP/6-311+G(d) calculations. From left to right, $n = 4$, 6, and 8. (Below) $n = 6$ highly symmetric structure.

to the cluster. No particular “magic numbers” are found in the growth pattern in this case, but the $n = 4$ cluster is found to be 20 kcal more stable than the average.

Theory: Quantum Structures. We optimized the structures of the cluster with $n = 2, 4, 6$, and 8 obtained with the MD technique illustrated above using DFT at the B3LYP/6-311+G(d) level (following a preoptimization with the smaller 6-311G(d) basis set), and we calculated the vibrational harmonic frequencies and the Raman intensities. It has been shown in previous studies^{54,55} on imidazolium- and piridinium-based ionic liquids that calculation of ionic pair binding energies should require ab initio-based calculations or, at least, dispersion-corrected DFT. Since we are here, in fact, only marginally interested in binding energies and considering that the dimension of the system precluded use of MP2 or other correlated methods, we employed the B3LYP functional which, as we show below, yields excellent agreement with the measured Raman spectra. The reasons why we decided to use clusters as a tool for investigation of the bulk compound are reported below:

- it is our opinion that they provide a fairly reliable description of a limited portion of the solid/liquid bulk phase without the need of performing Car–Parrinello ab initio dynamics which would be well beyond our computational facilities,
- already in the very small clusters with 4 ionic couples we see formation of a strong network of H bonds,
- many of the structural features of the liquid or solid phases depend on the short-range local geometric feature of the environment (especially infrared or Raman absorptions positions and intensities),
- while the “classical” treatment above has certainly captured most of the bonding features that characterize these systems, it is clear that a quantum refinement of the energetic network at play is necessary especially in view of the study of the weak interaction as the H-bonding features.

The resulting optimized structures are reported in Figure 8. As can be seen, although we used the “classical” structures as starting points, we obtained new geometries with quite a few important differences. For the $n = 6$ case, in addition to the structure with a centered NO_3^- we found a second possible structure where two

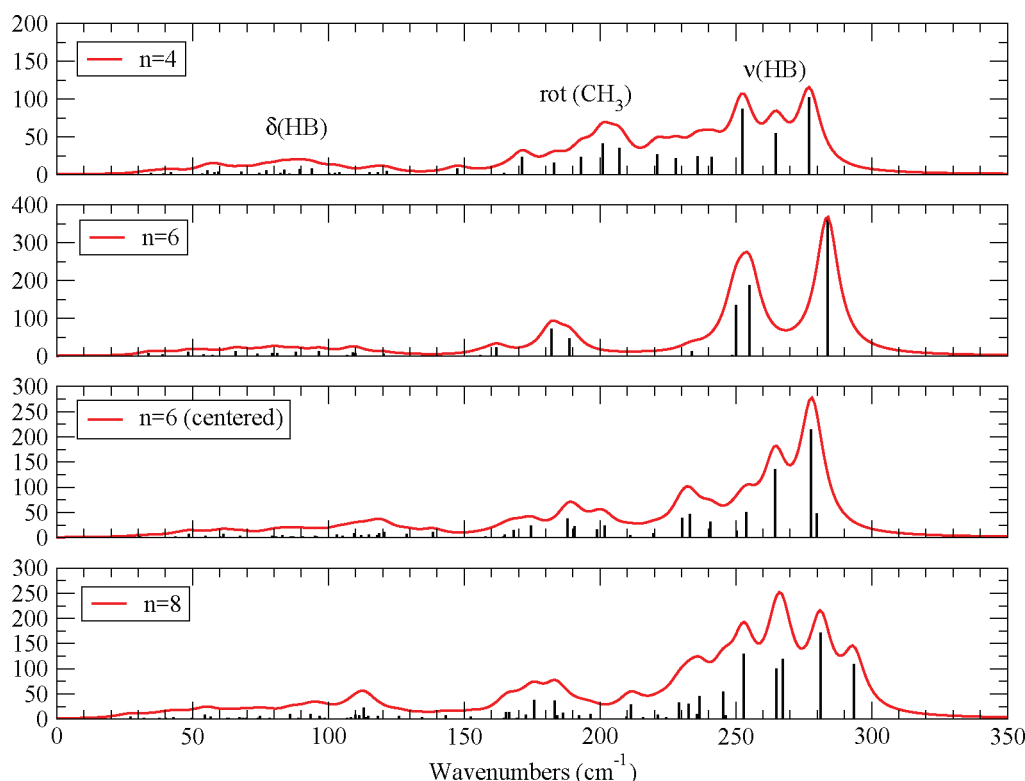


Figure 9. Simulated IR absorption spectra in the harmonic approximation for the 4 clusters at low frequencies.

cubic cages are formed with high symmetry. The latter is however less stable than the former one. In the case of $n = 4$ the high symmetry of the cluster is lost (we performed the quantum optimization in the C_1 point group, i.e., with no symmetry constraints). The cubic-like cage structures are also less clear in $n = 6$ and 8 , but more important, the local H-bond coordination is different: in the QM structures we found that a single nitrate ion often coordinates only two H bonds, whereas in the classical structures it saturated the three acceptor sites. Moreover, the average $N \cdots O$ distance is significantly larger, around 2.8 – 2.9 Å, which turns out to be in agreement with the diffraction data reported above and with recently published data.³⁵ In particular, the diffraction data reported above clearly identify two different types of $N-H \cdots O$ contacts (see Table 4): the first one is characterized by an angle of $\sim 167^\circ$, whereas the second has a greater deviation from linearity, forming an angle of about 156° . It is interesting to note that the donor–acceptor distances are almost the same. As a result of the different angle, the $N-O$ distance in the nitrate group is slightly different: $N(1)-O(1) = 1.200(6)$ Å and $N(1)-O(2)(\times 2) = 1.243(4)$ Å. This shortening of one of the three $N-O$ distances on the nitrate group is also seen in the ab initio structures where we find that the shortest one (about 1.22 Å) corresponds to $N-O$ which are not forming an H bond while the longest one (about 1.25 Å) is involved in highly directional H bonds. Therefore, we find that there is a sizable weakening of the $N-O$ bond when it is involved in an H bond that results in an elongation of 0.03 – 0.04 Å. Note that this behavior is also in agreement with what has been found in ref 34 by means of a Car–Parrinello approach where 1.82 H bonds were found for each nitrate and the radial distributions functions confirm the larger average acceptor donor distance even with the constant volume constraint. This means that the

“classical” calculations with the OPLS force fields reported above are overestimating the H-bond forces and that a proper quantum treatment is necessary to provide a realistic picture of the cluster behavior and, presumably, of the liquid phase. By performing BSSE counterpoise calculations on the optimized geometries we found that the interaction energy “per ionic couple” in the $n = 4$ cluster is 137.3 kcal, 152.17 kcal for $n = 6$, and 154 kcal for $n = 8$. These values are consistent with the “classical” one of 141 kcal.

In order to provide a possible scheme for creating a new force field for these compounds we report the electrostatic potential fitting charges as obtained at our level of calculations with the CHELPG procedure. The nitrate has a global charge of 0.63 – 0.74 , where the N atom has a charge of 0.90 – 0.98 and the O atom a negative charge of 0.53 – 0.57 . The methylammonium has an almost neutral methyl group (we find a charge of 0.07 – 0.08), while NH_3^+ is positively charged with 0.62 – 0.66 , although the partial atomic charge on the ammonium N is fluctuating from almost neutral to $+0.4$. These calculations show that in the present systems there is a limited but sizable polarization effect and that the two ions are not carrying a unit charge.

In Figure 9 we report the low-energy harmonic frequencies as calculated at the equilibrium geometries for the 4 quantum structures. In this region it is possible to find the vibrational absorption bands typical of the intermolecular interactions in the cluster. In particular, between 150 and 300 cm^{-1} we see a series of absorptions that can be assigned to H-bond stretching (both symmetric and asymmetric) and rotation of the CH_3 groups (with frequencies around 160 – 180 cm^{-1}). The lower frequencies contain few modes that can be described as H-bond bending motions. This part of the spectra is extremely sensitive to the

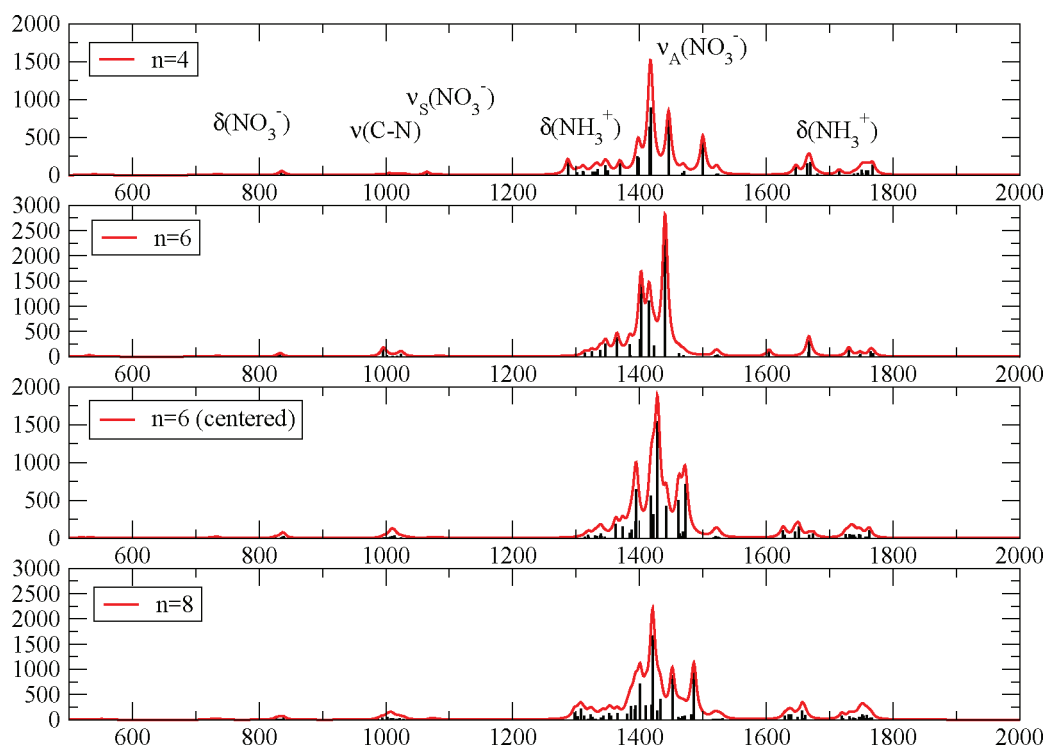


Figure 10. Simulated IR absorption spectra in the harmonic approximation for the 4 clusters at intermediate frequencies.

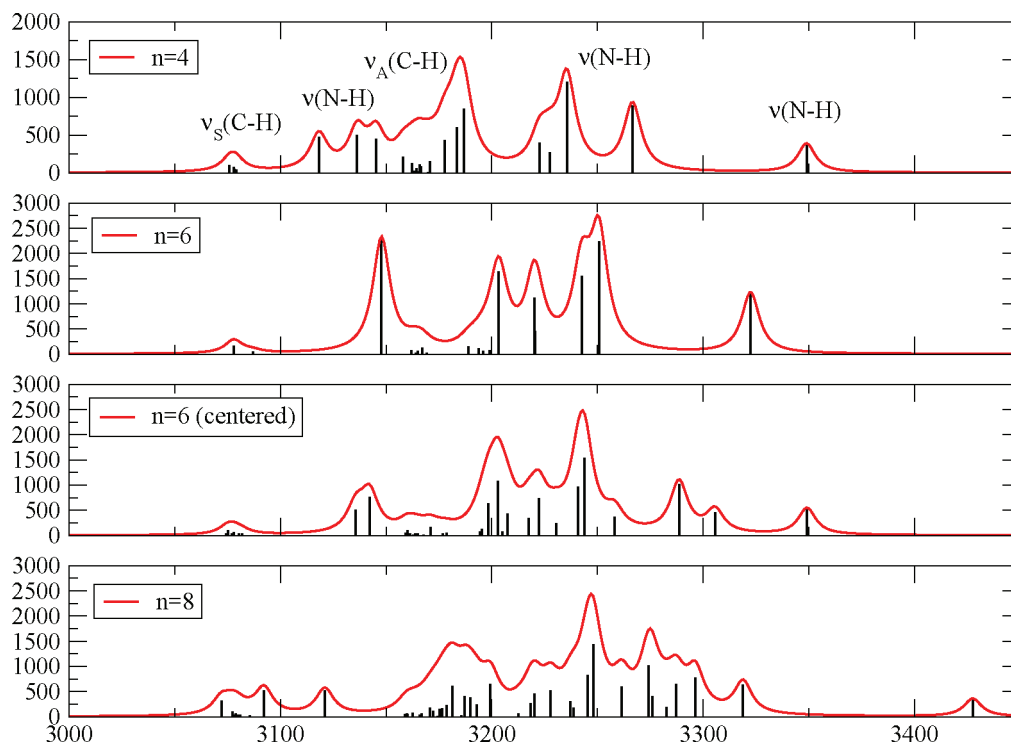


Figure 11. Simulated IR absorption spectra in the harmonic approximation for the 4 clusters at high frequencies.

global structure of the cluster as shown by the significant differences between the two spectra relative to the $n = 6$ structures; therefore, it has been partially exploited to characterize the H-bonding network in ethylammonium and dimethylammonium nitrate.^{56,57}

In Figure 10 we report the medium-frequency range where we can assign weak bending motions of the NO_3^- ion at 730 (in-plane bending) and 830 (out-of-plane bending) cm^{-1} . The symmetric stretching of NO_3^- is found as a weak band around 1060–1080 cm^{-1} , preceded by the equally weak C–N stretching

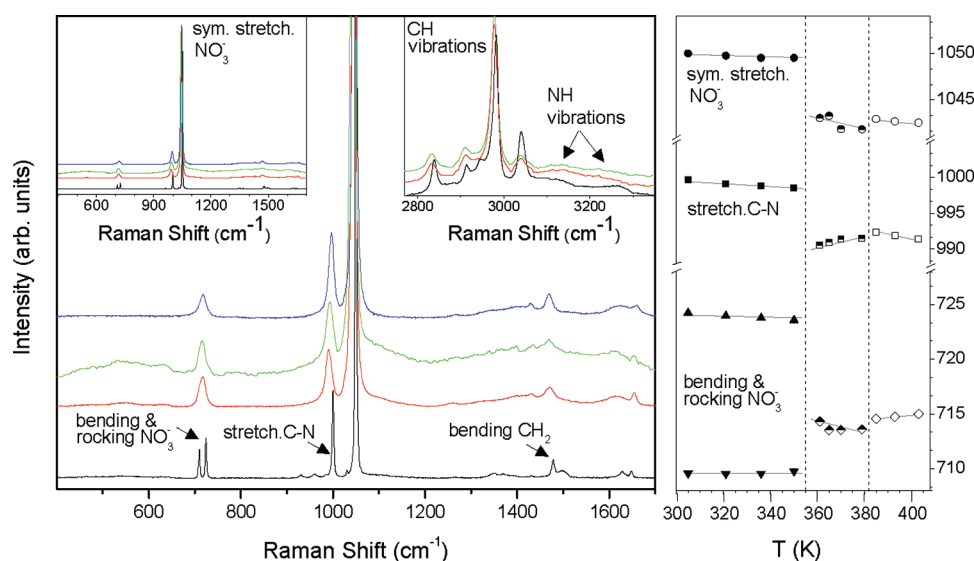


Figure 12. (Left) Raman spectra of MMAN under different thermodynamic conditions and over different spectral regions. From bottom to top: solid II (RT in black), solid I ($T = 354$ K, in red), liquid ($T = 390$ K, in green), and in water solution (RT, $R = 7$, in blue). The main panel is an expanded view of the low-frequency region shown in the upper left panel. The upper right panel shows the high-frequency region. (Right) Temperature dependence of selected mode frequencies on the low-frequency region.

modes. High absorptions are seen for the bending modes of NH_3^+ between 1280 and 1360 cm^{-1} , the asymmetric stretching of NO_3^- (1400 – 1445 cm^{-1}), and the pyramidal and scissoring motions of NH_3^+ around 1650 and 1750 cm^{-1} , respectively.

At higher frequencies (Figure 11) we can see that while the stretching of the CH_3 group produces two distinct sets of absorptions very similar to each other that correspond to asymmetric and symmetric motions, the $\text{N}(+)-\text{H}$ stretching produces a complex pattern which gives rise to a series of absorptions ranging from the higher frequencies for $\text{N}-\text{H}$ almost not involved in H bonding to 3100 cm^{-1} for those more strongly bound to the $\text{N}-\text{O}$ acceptor.

Raman Spectra. Raman spectra collected from solid II, solid I, and liquid MMAN are shown in Figure 12 (left). On the right of Figure 12 the temperature dependence of the first three structures on the low-frequency side of the spectrum is shown. Raman spectra have also been collected on several MMAN–water solutions at different concentrations. The latter measurements are basically identical regardless of the concentrations investigated. For this reason, only a representative spectrum collected from a MMAN–water solution ($R = 7$, where $R = [\text{H}_2\text{O mol}]/[\text{MMAN mol}]$) is shown on the left of Figure 12. According to refs 58 and 59 the assignment of the major Raman peaks to vibrational modes of MMAN is given by the labels shown in the figure.

Looking at Figure 12 it is well evident that the Raman spectrum of the solid II MMAN is remarkably different from the others. In particular, the transition from the orthorhombic to the cubic phase of solid I is clearly indicated by the transformation of the doublet at around 700 cm^{-1} ascribed to NO_3^- cation vibrational modes into a single peak, coherently with achievement of the more symmetric structural phase. The clear broadening of the Raman peaks on entering the high-temperature phases (solid and liquid) can be safely ascribed to an increase of the structural disorder, although, generally speaking, peak broadening can be also ascribed to a temperature increase. The disorder-induced origin of the broadening is indeed supported

by the observation of similarly large line widths in the Raman spectrum of the MMAN–water solution which was collected at ambient temperature. On the other hand, this finding is in agreement with the interpretation suggested by the present X-ray data where the increase of the background signal is ascribed to the more disordered solid I phase. The presence of structural disorder in solid I, as we pointed out above, has been also previously reported in ref 33, where rapid rotations of anions and cations around the $\text{C}-\text{N}$ axis in both solid I and liquid have been deduced from analysis of NMR data.

The temperature dependence of selected Raman peaks is shown on the right panel of Figure 12. The overall weak decreasing trend of the peak frequencies can be ascribed to the previously discussed temperature-induced lattice expansion. The guides to the eye point out two different behaviors above and below the solid II–solid I transition temperature from the orthorhombic to the cubic solid. The sharp softening of the frequencies on entering the solid I phase can be mainly related to the abrupt 3.5% volume expansion determined by the X-ray diffraction experiment. When crossing the melting temperature, discontinuities in the pressure dependence of the main vibrational frequencies are also observed, albeit of much smaller extent than those observed at the solid–solid transition. In particular, a small jump toward higher values can be indeed observed in the frequencies of the vibrational modes related to the NO_3^+ ion. Bearing in mind the above-mentioned weakening of the $\text{N}-\text{O}$ bond when it is involved in an H bond, the observed behavior on melting can indicate the weakening of the H bond in the liquid phase. We want to emphasize that although most of the Raman peaks measured can be mainly ascribed to internal vibrational modes of the two ions, their significant sensitivity to volume variation indicates that the vibrational spectrum is also a sensible probe of the ion–ion interaction. All of the above findings together with the apparent strong similarity among the spectra collected from the solid I and liquid phases and from the water solution strongly support the idea that MMAN adopts a similar local structure in all these phases. On this basis, a local isotropic

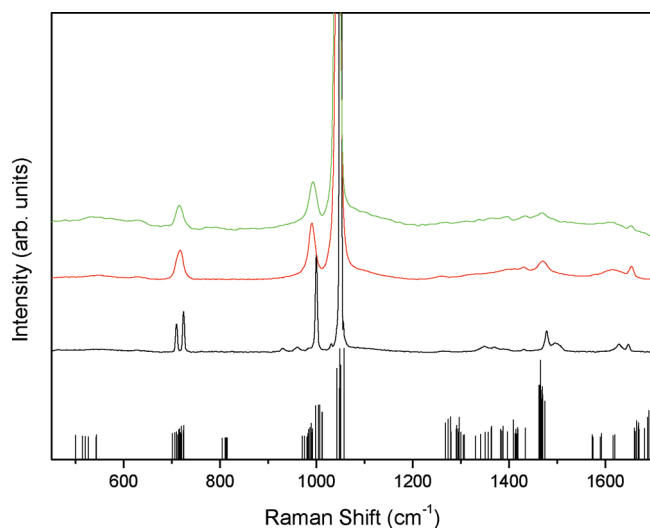


Figure 13. Experimental and calculated Raman spectra of MMAN, from bottom to top: calculated intensities of the vibrational modes (six ionic couples model) with energy scaled by 0.964 and on a logarithmic y axis, solid II at RT (black), solid I at $T = 354$ K (red), and liquid at 390 K (green).

configuration accompanied by a remarkable level of anion/cation orientational disorder can be conjectured for MMAN at these thermodynamic conditions. It is worth noticing the apparently weak role played by the polar solvent (water) which basically does not affect the anion–cation correlation.

In Figure 13 the comparison between the experimental Raman spectra of MMAN (solid II, solid I, and liquid) and the calculated theoretical spectrum (only calculated mode intensities) obtained with the six anion/cation cluster is shown. It is clear that theoretical calculations are able to reproduce the main structures of the experimental Raman spectrum. Bearing in mind that the single-ion contributions to the Raman spectrum of MMAN are particularly relevant, the above agreement indicates that the theoretical model adopted well reproduces the intramolecular vibrations. Intermolecular motions absorb at very low frequencies, and we do not have reliable data in that region. The intramolecular interactions, however, leave their imprints on the high- and intermediate-energy scale motions by modifying the vibrational constants of various motions. For example, in the high-frequency domain, a better agreement with the theoretical calculations is found with the experimental spectra measured from the samples in the solid I and liquid phases.

The high-energy region of the spectra from theoretical calculations is reported in Figure 11. The $\text{N}^+ \text{--} \text{H}$ donor site which does not form an H bond appears in the IR/Raman spectra above 3300 cm^{-1} . The other absorption bands between 3150 and 3300 cm^{-1} are due to different $\text{N}^+ \text{--} \text{H}$ stretching motions distributed along the frequency scale because of the different strengths of the H bond in which they are involved. Two distinct broad features typical of $\text{N}^+ \text{--} \text{H}$ motions can be spotted in the experimental Raman spectra: one at $3100\text{--}3150 \text{ cm}^{-1}$ and another at 3250 cm^{-1} . The latter is clearly visible in the solid II phase spectra, while it is hardly detectable in the disordered phases of the higher temperatures. We surmise that this spectral feature is due to the following situation: although in the solid II phase all the $\text{N}^+ \text{--} \text{H}$ donor sites form an H bond, X-ray analysis reported above shows that there are two types of H bonds.

Since one of the three $\text{N}^+ \text{--} \text{H}$ donor sites has a contact with an oxygen of the nitrate anion which is due to a weaker H bond than the other two, there exist two different absorption peaks in the Raman spectra in the $\text{N}^+ \text{--} \text{H}$ region. When we move to the more disordered solid I and liquid phases, this effect tends to cancel and we see, instead, a more broad distribution of absorption frequencies which is probably due to a distribution of H-bonding strengths.

CONCLUSIONS AND PERSPECTIVES

In the present work we reported an investigation of the structure of the MMAN molten salt using different experimental techniques and ab initio computations. First, we characterized by powder X-ray scattering experiments the two solid phases and found that the one that exists at high temperature is a polymorph and has a high degree of disorder. This phase is probably what is commonly known as an ionic plastic where the ions retain a more or less fixed reticular position though they undergo coupled end-over-end rotational motions. This fact is confirmed by the findings we collected with Raman spectroscopy where we found a strong similarity between the spectra of this plastic phase with those of the high-temperature liquid one. In order to provide a structural interpretation of these disordered phases we performed a series of calculations on clusters composed by a small number of ionic couples. We have seen how the ab initio optimizations produce slightly asymmetrical structures in which the presence of H-bonding features is determinant in producing the spatial arrangement of the molecular partners. We calculated the Raman spectra for a few of the optimized clusters and compared them with the experimental ones: the agreement in the intermediate- and high-frequency range is very encouraging, and we were able to assign most of the experimental peaks. The proposed microscopic structures present various features that compare well with previous and present experimental and theoretical findings: for example, we see that in our simulated clusters not all the NO_3^- acceptor sites are saturated by an H bond as previously found by ab initio MD³⁴ and as further confirmed by the present X-ray scattering analysis. Moreover, thanks to a comparison with the calculated spectra, we interpreted the appearance of a double-peak feature in the high-frequency region of the Raman spectra of the solid II phase as a consequence of the existence of two different H bonds in which one of the $\text{N}^+ \text{--} \text{H} \cdots \text{O}$ contacts is mediated by a weaker bond. This double feature almost disappears in the more disordered phases.

AUTHOR INFORMATION

Corresponding Author

*E-mail: bodo@caspur.it.

ACKNOWLEDGMENT

Financial support from the Scientific Committee of the University of Rome is gratefully acknowledged. Computational support of the CASPUR and CINECA Supercomputing Centers is also acknowledged.

REFERENCES

- (1) Stark, A.; Seddon, K. R. In *Kirk-Othmer Encyclopaedia of Chemical Technology*, 5th ed.; Seidel, A., Ed.; John Wiley & Sons, Inc.: Hoboken, NJ, 2007; Vol. 26, pp 836–920.
- (2) Freemantle, M. *An Introduction to Ionic Liquids*; RSC Publishing, 2009; p 281.

- (3) Plechkova, N. V.; Seddon, K. R. *Chem. Soc. Rev.* **2008**, 37, 123–150.
- (4) In *Ionic Liquids Synthesis*, 2nd ed.; Welton, T., Wasserscheid, P., Eds.; Wiley VCH: Weinheim, 2008; p 721.
- (5) In *Ionic Liquids IIIA: Fundamentals, Progress, Challenges, and Opportunities: Properties and Structure*; Rogers, R. D., Seddon, K. R., Eds.; ACS Symposium Series 901; American Chemical Society: Washington, D.C., 2005; p 356.
- (6) In *Ionic Liquids: From Knowledge to Application*; Rogers, R. D., Plechkova, N. V., Seddon, K. R., Eds.; ACS Symposium Series 1030; American Chemical Society: Washington, D.C., 2009; p 464.
- (7) Forsyth, S. A.; Pringle, J. M.; MacFarlane, D. R. *Aust. J. Chem.* **2004**, 57, 113–119.
- (8) Zeng, Z.; Phillips, B. S.; Xiao, J.-C.; Shreeve, J. M. *Chem. Mater.* **2008**, 20, 2719–2726.
- (9) Hough, W. L.; Rogers, R. D. *Bull. Chem. Soc. Jpn.* **2007**, 80, 2262–2269.
- (10) Hough, W. L.; Smiglak, M.; Rodriguez, H.; Swatloski, R. P.; Spear, S. K.; Daly, D. T.; Pernak, J.; Grisel, J. E.; Carliss, R. D.; Soutullo, M. D.; Davis, J. H., Jr.; Rogers, R. D. *New J. Chem.* **2007**, 31, 1429–1436.
- (11) Mizuuchi, H.; Jaitely, V.; Murdan, S.; Florence, A. *Eur. J. Pharm. Sci.* **2008**, 33, 326.
- (12) Boon, J. A.; Levisky, J. A.; Pflug, J. L.; Wilkes, J. S. *J. Org. Chem.* **1986**, 51, 480–3.
- (13) Fischer, T.; Sethi, A.; Welton, T.; Woolf, J. *Tetrahedron Lett.* **1999**, 40, 793–796.
- (14) Wasserscheid, P.; Keim, W. *Angew. Chem., Int. Ed.* **2000**, 39, 3772–3789.
- (15) Welton, T. *Chem. Rev.* **1999**, 99, 2071–2083.
- (16) Koel, M. C. *Rev. Anal. Chem.* **2005**, 35, 177.
- (17) Tan, S. S. Y.; MacFarlane, D. R.; Upfal, J.; Edey, L. A.; Doherty, W. O. S.; Patti, A. F.; Pringle, J. M.; Scott, J. L. *Green Chem.* **2009**, 11, 339.
- (18) Sun, H.; Zhang, D.; Liu, C.; Zhang, C. *THEOCHEM* **2009**, 900, 37.
- (19) Buzzeo, M. C.; Evans, R. G.; Compton, R. G. *ChemPhysChem* **2004**, 5, 1106.
- (20) Endres, F.; Abedin, S. Z. E. *Phys. Chem. Chem. Phys.* **2006**, 8, 2101.
- (21) Hapiot, P.; Lagrost, C. *Chem. Rev.* **2008**, 108, 2238.
- (22) MacFarlane, D. R.; Forsyth, M.; Howlett, P. C.; Pringle, J. M.; Sun, J.; Annat, G.; Neil, W.; Izgorodina, E. I. *Acc. Chem. Res.* **2007**, 40, 1165.
- (23) Maginn, E. J. *J. Phys. Condens. Matter* **2009**, 21, 373101.
- (24) Angell, C. A.; Byrne, N.; Belieres, J.-P. *Acc. Chem. Res.* **2007**, 40, 1228–1236.
- (25) Greaves, T. L.; Drummond, C. J. *Chem. Rev.* **2008**, 108, 206–237.
- (26) Xu, W.; Angell, C. A. *Science* **2003**, 302, 422–425.
- (27) Yoshizawa, M.; Xu, W.; Angell, C. A. *J. Am. Chem. Soc.* **2003**, 125, 15411–15419.
- (28) Nakamoto, H.; Watanabe, M. *Chem. Commun.* **2007**, 2539–2541.
- (29) Atkin, R.; Warr, G. G. *J. Phys. Chem. B* **2008**, 112, 4164–4166.
- (30) Greaves, T. L.; Weerawardena, A.; Krodziewska, I.; Drummond, C. J. *J. Phys. Chem. B* **2008**, 112, 896–905.
- (31) Mamontov, E.; Luo, H.; Dai, S. *J. Phys. Chem. B* **2009**, 113, 159–169.
- (32) Walden, P. *Bull. Acad. Imper. Sci. (St. Petersburg)* **1914**, 1800.
- (33) Wasylishen, R. E. *Can. J. Chem.* **1986**, 64, 773.
- (34) Zahn, S.; Thar, J.; Kirchner, B. *J. Chem. Phys.* **2010**, 132, 124506.
- (35) Zahn, S.; Wendler, K.; Delle Site, L.; Kirchner, B. *Phys. Chem. Chem. Phys.* **2011**, 13, 15083–15093.
- (36) Petricek, V.; Dusek, M.; Palatinus, L. *JANA2006*; Institute of Physics: Praha, Czech Republic, 2006.
- (37) Mylrajan, M.; Srinivasan, T. K. K.; Sreenivasamurthy, G. *J. Cryst. Spectr. Res.* **1985**, 15, 493.
- (38) Gonschorek, W.; Schmahl, W. W.; Weitzel, H.; Miehe, G.; Fuess, H. *Z. Kristallogr.* **1995**, 210, 843.
- (39) Ballirano, P.; Melis, E. *Phys. Chem. Miner.* **2007**, 12, 289–295.
- (40) Larson, A. C.; Von Dreele, R. B. *GSAS-General Structure Analysis System*; Los Alamos National Laboratory Report No. LAUR 86-748. Los Alamos National Laboratory: Los Alamos, 2000.
- (41) Toby, B. H. *J. Appl. Crystallogr.* **2001**, 34, 210.
- (42) Thompson, P.; Cox, D. E.; Hastings, J. *J. Appl. Crystallogr.* **1987**, 20, 79.
- (43) Finger, L.; Cox, D.; Jephcoat, A. *J. Appl. Crystallogr.* **1994**, 27, 892–900.
- (44) Topas, B. A. *V4.2: General profile and structure analysis software for powder diffraction data*; Bruker AXS: Karlsruhe, Germany, 2009.
- (45) Robert, C.; Casella, G. *Monte Carlo Statistical Methods*; Springer-Verlag, 2004.
- (46) Hartke, B. *J. Phys. Chem.* **1993**, 97, 9973–9976.
- (47) Jorgensen, W. L.; Maxwell, D. S.; Tirado-Rives, J. *J. Am. Chem. Soc.* **1996**, 117, 11225–11236.
- (48) Lebrero, M. C. G.; Bikiel, D. E.; Elola, M. D.; Estrin, D. A.; Roitberg, A. E. *J. Chem. Phys.* **2002**, 117, 2718–2725.
- (49) <http://dasher.wustl.edu/tinker/>.
- (50) Frisch, M. J.; et al. *Gaussian 09*, Revision A.1; Gaussian Inc.: Wallingford, CT, 2009.
- (51) Mallinson, P. R.; Koritsanzky, T.; Elkaim, E.; Li, N.; Coppens, P. *Acta Crystallogr.* **1998**, A44, 336.
- (52) Gonschorek, G.; Weitzel, H.; Miehe, G.; Fuess, H.; Schmahl, W. W. *Z. Kristallogr.* **2000**, 215, 752.
- (53) Chio, C. S.; Prask, H. J.; Prince, E. *J. Appl. Crystallogr.* **1980**, 13, 403.
- (54) Izgorodina, E. I.; Bernard, U. L.; MacFarlane, D. R. *J. Phys. Chem. A* **2009**, 113, 7064–7072.
- (55) Zahn, S.; Kirchner, B. *J. Phys. Chem. A* **2008**, 112, 8430–8435.
- (56) Fumino, K.; Wulf, A.; Ludwig, R. *Angew. Chem., Int. Ed.* **2009**, 48, 3184–3186.
- (57) Wulf, A.; Fumino, K.; Ludwig, R. *Angew. Chem., Int. Ed.* **2010**, 49, 449–453.
- (58) Mylrajan, M.; Srinivasan, T. *J. Raman Spectrosc.* **1985**, 16.
- (59) Mylrajan, M.; Srinivasan, T. *J. Raman Spectrosc.* **1987**, 18.